THE JOURNAL OF PHYSICAL CHEMISTRY C

ARTICLE

pubs.acs.org/JPCC

Why Silver Nanoparticles Are Effective for Olefin/Paraffin Separations

Zachary D. Pozun, Kelly Tran, Anna Shi, Ryan H. Smith, and Graeme Henkelman*

Department of Chemistry and Biochemistry and the Institute for Computational Engineering and Sciences, University of Texas at Austin, 1 University Station A5300, Austin, Texas 78712-0165, United States

ABSTRACT: The majority of nanocomposite olefin/paraffin separation membranes use silver nanoparticles or silver ions as the olefin binding agent. In this theoretical study, we characterize the olefin interaction with silver nanoparticles and show that silver is special in that it chemisorbs ethylene more weakly than other metals. Some variation with particle size is found; small 79 atom nanoparticles tend to bind ethylene more strongly than larger 140 atom particles, which in turn are well approximated by facets of bulk crystal surfaces. The effect of replacing cores of nanoparticles with different metals is demonstrated to selectively tune binding based on the relative *d*-band centers of the two metals. We identify silver-cored, gold-shelled nanoparticles as potentially more effective for olefin/paraffin separations. Random alloys of gold and silver were also considered. We find that 25%−75% Au−Ag random alloys are strong candidates for use in olefin/paraffin separation membranes due to the presence of reactive (111) faces without the cost of a strong increase in the binding energies on edges and corners. Nanocomposite membranes containing these nanoparticles hold promise for more efficiently separating olefins from paraffins.

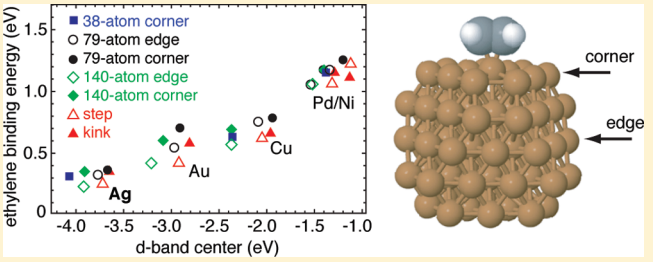

INTRODUCTION

Ethylene, a basic industrial synthetic building block, is commonly used in the production of various polyethylene plastics as well as in many glycols, surfactants, and styrenes. With yearly production exceeding 75 million tons, ethylene is the most commonly produced light olefin.[1] Ethylene and other light olefins are typically produced via steam cracking of naphtha, ethane, and other hydrocarbon feeds at high temperatures.[2] Steam cracking, including related purification processes, is the most energy intensive processes in the petrochemical industry.[3]

The separation from ethane is a key step in the production of ethylene via steam cracking. Typically, ethylene/ethane mixtures are liquified for cryodistillation in large fractionating columns. This process, in large part due to the required phase change, is highly energy-intensive. Olefin/paraffin separation accounts for well over 10^{14} BTU of energy per year.[4] Gas separation membranes offer an appealing energy-efficient alternative to the cryodistillation process.

Olefin/paraffin separation membranes commonly contain silver ions that selectively chemisorb olefins.[5−8] Membranes containing silver ions are unstable over long periods of time and under exposure to light.[9] Membranes that replace ionic silver with silver nanoparticles have been demonstrated to be more resistant to degradation over time while remaining selective for olefins.[10,11] Similar membranes containing gold nanoparticles in place of silver have also been demonstrated to be selective for propylene over propane.[12]

Models of olefin/paraffin separation indicate that the selective properties of nanocomposite membranes may be tuned by adjusting the binding energy of the olefin onto nanoparticles.[13] Nanoparticles are particularly appealing for this type of application because their properties, such as the binding energy of a target molecule, may be tuned by adjusting the particle size and composition.[14] Beginning with the unusual size dependence of catalytically active Au nanoclusters by Valden et al.,[15] size effects in nanoparticles have been of considerable interest for catalyst design. Size represents a tunable parameter that may be controlled experimentally in order to adjust the binding energy of ethylene to the nanoparticle surface.

Bimetallic systems offer a second level of tuning—in addition to particle size—to selectively increase or decrease the surface electron density by substituting a more electron-rich or electron-poor metal at the near-surface.[16,17] Core−shell bimetallic nanoparticles can be synthesized using dendrimer encapsulation techniques with controlled size and composition.[18,19]

In this work, we seek to identify the properties of Ag that contribute to its uniqueness for olefin/paraffin separation membranes. We find that Ag is special, for it has the weakest chemisorption energy for ethylene among the late transition metals. We then investigate alloys to find other possible nanoparticles with chemisorption energy similar to, or weaker than, Ag. Ultimately, we suggest novel nanoparticles that could potentially improve upon the effectiveness of Ag for use in olefin/paraffin separation membranes.

COMPUTATIONAL DETAILS

The chemisorption of ethylene to noble metal nanoparticles and slabs was calculated with density functional theory (DFT). The coinage metals of group 11—Cu, Ag, and Au—as well as the

Received: November 5, 2010
Revised: December 15, 2010
Published: January 10, 2011

ACS Publications © 2011 American Chemical Society

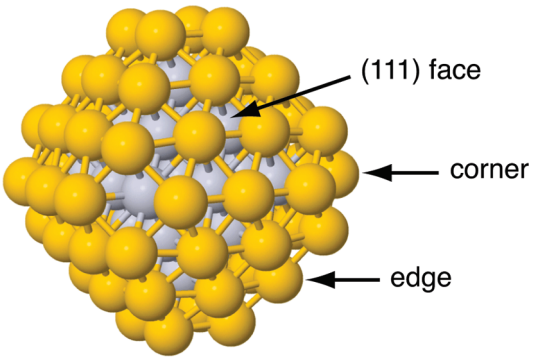

Figure 1. A 79-atom Ag@Au core−shell nanoparticle; binding sites for ethylene are shown.

group 10 metals—Ni, Pd, and Pt—were considered as pure metal, core-shell, and random alloy nanoparticle geometries. Ethylene binding to metal slabs at kink and step defects was also considered.

All DFT calculations were performed using the Vienna *ab initio* Simulation Package (VASP).[20] Valence electrons were described with Kohn−Sham single-electron wave functions[21,22] and expanded in a plane wave basis with an energy cutoff of 274 eV. Core electrons, including the semicore p states in the metals, were described within the projector augmented wave (PAW) framework.[23,24] Spin-polarization was considered in all cases and applied where required. The exchange-correlation contribution to the DFT energy was determined through the PW91 generalized-gradient approximation (GGA) functional.[25]

DFT was used to optimize the structure of all nanoparticles, adsorbates, and surfaces such that the forces on all atoms were less than 0.01 eV/Å. Nanoparticle structures, containing 38, 79, or 140 atoms, were assumed to be in a face-centered cubic truncated-octahedron geometry. In core−shell nanoparticle geometries, the 6, 19, and 44 core atoms were replaced by a different metal. Alloy nanoparticles were generated by randomly distributing specified fractions of the component metal atoms in the nanoparticle.

Nanoparticles were placed in the simulation box with a 4 Å vacuum on all sides such that periodic images were separated by at least 8 Å. The Brillouin zone was sampled at the Γ-point, and a Gaussian-like function[26] with a smearing width of 0.01 eV was used for determining partial occupancies of states near the Fermi level. Binding sites included (111) faces and edge and corner sites and are shown on a $Ag_{19}@Au_{60}$ nanoparticle in Figure 1. The notation is of the form core@shell.

Slab calculations were performed on FCC surfaces with the bottom two layers held frozen in bulk positions using PAW-GGA optimized lattice constants.[27] A vacuum of at least 10 Å was used to separate periodic images between slabs. The Brillouin zone was sampled with a 4 × 4 × 1 Monkhorst-Pack[28] *k*-point mesh and integrated using the method of Methfessel and Paxton[29] with a smearing width of 0.1 eV. For both nanoparticle and slab systems, the energy was extrapolated to a state of no partial occupancy.

The clean (111) face was modeled in a p(3 × 3) geometry, with nine atoms per layer. The stepped surface, similar to the nanoparticle edge, has a (111) microfacet. The slab analogue of a corner binding site was chosen as a kink site on the (111) surface. The step and kink binding sites are shown in Figure 2. Both the stepped and kinked surfaces were modeled using vicinal surfaces and sampled with the same *k*-point mesh as the clean slab.

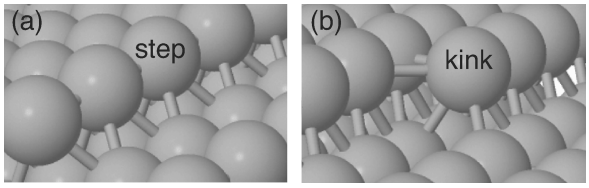

Figure 2. (a) A (111)/(111) step is the binding site analog of a nanoparticle edge site. (b) A kink site is the slab analogue of a nanoparticle corner site.

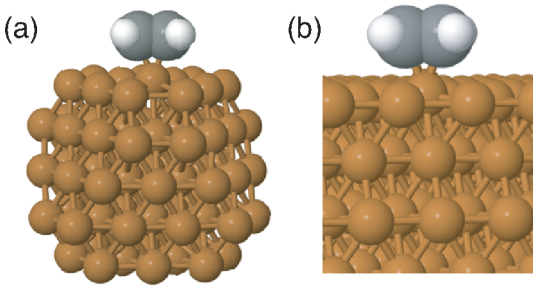

Figure 3. Ethylene binding (a) atop a single Cu atom on the (111) face of a Cu_{79} nanoparticle and (b) on the bulk Cu(111) surface.

The local *d* density of states (DOS) was calculated for each atom by projecting the Kohn−Sham wave functions onto spherical harmonic functions within the atom's Bader volumes.[30] A grid-based decomposition of the charge density was used to determine the Bader volume.[31] The *d*-band center was determined by an average over the range −10 to 2 eV with respect to the Fermi level.

For vibrational frequencies, the Hessian matrix was built by moving all atoms in the ethylene molecule and the nearby metal atoms by a finite difference of 0.002 Å. The Hessian was then diagonalized to find the normal modes. Due to the accurate forces required to build the Hessian, systems where vibrational frequencies were calculated were further optimized in geometry such that the force per atom was smaller than 0.003 eV/Å.

■ ETHYLENE BINDING ON PURE METALS

(111) Faces. Molecular binding on (111) faces tends to be weak; the surface electronic states are delocalized over the surface and the overlap between the adsorbate HOMO and the surface is small. The high coordination of surface atoms delocalizes the surface states in contrast to a rough surface with localized states where stronger binding can occur.[32]

The binding geometries of ethylene at nanoparticles and slabs are shown in Figure 3. On the (111) face, the molecule sits directly on top of a single surface atom; this binding position has been determined theoretically for Cu,[33,34] Ag,[35] and Au.[32] Small nanoparticles have small (111) faces over which electronic states may be delocalized. With increasing size, the faces grow larger and allow for a greater degree of delocalization of states. The effect of size on chemisorption on the (111) face is shown in Table 1.

From Table 1, small nanoparticles—those containing 38 and 79 atoms—tend to bind ethylene stronger than larger particles. There is only small variation between the 140-atom nanoparticles and the bulk value. No chemisorption is found for any size for

Table 1. Ethylene Binding to (111) Faces (eV)

	NP-38	NP-79	NP-140	slab
Ni	0.94	0.73	0.77	0.72
Pd	0.65	0.74	0.75	0.78
Pt	1.35	1.24	0.99	0.89
Cu	0.11	0.29	0.14	0.21
Ag	*a*	*a*	*a*	*a*
Au	*b*	0.25	0.10	0.10

[a] No chemisorptive interaction >0.05 eV. [b] Particle deformed.

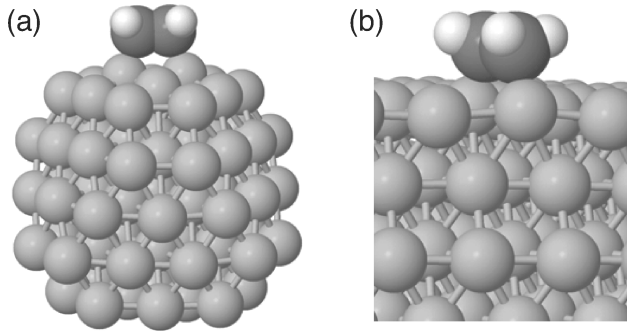

Figure 4. The di-σ bridging geometry for ethylene (a) on a $Pt_{79}(111)$ face and (b) on bulk Pt(111).

Table 2. Di-σ (111) Face Binding (eV)

	NP-38	NP-79	NP-140	slab
Pd, di-σ	1.00	0.96	1.02	1.00
Pt, di-σ	1.59	1.59	1.35	1.18

Ag nanoparticles or on the bulk, and only weak binding is seen for large Au particles and the surface of Au(111). The Ni group metals all chemisorb ethylene stronger than the Cu group.

The binding energies in Table 1 are for the top site binding position; however, experimental[36] and theoretical[37,38] evidence indicates that, on the Pt(111) face, ethylene chemisorbs preferentially through a di-σ interaction. In this geometry, the carbon centers become sp^3-like as the molecule bridges two surface Pt atoms.[37] This is in contrast to the top-site binding where the center of the C−C bond is on top of a single surface atom and both carbon atoms remain sp^2-like in character. The same preference for di-σ surface binding compared to top binding is observed for ethylene chemisorption on the Pd(111) face[38,39] and Pd(100) face.[40,41]

The di-σ binding geometries are shown in Figure 4 and energies in Table 2. Chemisorption on Pt and Pd is preferred in the di-σ binding geometry. Top site binding from Table 1 is unfavorable as compared to the di-σ geometry at all sizes.

Edges and Steps. Edge and corner atoms, as well as their slab analogues, are under-coordinated as compared to the bulk. Under-coordination localizes electronic states at the defect and allows for greater overlap between the adsorbate HOMO and the surface LUMO.[33,34,42] Ethylene chemisorption to edge sites is shown in Figure 5, and the binding energies are summarized in Table 3. There are no edge atoms in the 38-atom nanoparticles.

From Table 3, several trends emerge. Once the particle size reaches 140 atoms, the binding energies are, in general, close to

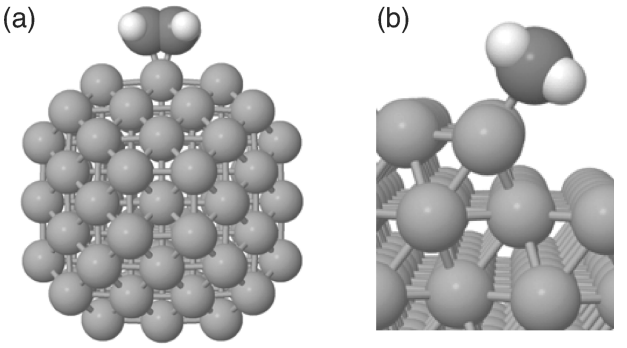

Figure 5. Ethylene binding (a) to a Ag_{79} nanoparticle edge and (b) to a step on Ag(111)/(111).

Table 3. Edge and Step Site Binding (eV)

	NP-79	NP-140	slab-step
Ni, π	1.17	1.26	1.23
Pd, di-σ	1.28	1.25	1.16
Pd, π	1.05	1.06	1.07
Pt, di-σ	1.73	1.51	1.40
Pt, π	1.37	1.23	1.18
Cu, π	0.75	0.57	0.63
Ag, di-σ	*a*	*a*	*a*
Ag, π	0.32	0.23	0.26
Au, di-σ	0.45	0.36	0.26
Au, π	0.43	0.42	0.43

[a] No chemisorptive interaction >0.05 eV.

the bulk equivalent values. Small particles, those with 38 and 79 atoms, bind ethylene more strongly. The di-σ binding geometry is dominant at all sizes for Pd and Pt, but the π geometry dominates for the other metals. Uniquely among these metals, Ag has no di-σ chemisorption.

Corners and Kinks. The under-coordinated atoms at corners and kinks have localized electronic states and are generally free of steric hindrance from neighboring atoms, so binding is expected to be strongest on these sites. Ethylene chemisorption is shown in Figure 6, and the binding energies are summarized in Table 4.

Binding is the strongest on the corners and kinks as compared to edges and the (111) face. There is also less variation in binding energy across the range of particle sizes into the bulk. In particular, Ag, Pd, and Pt show almost no change with increasing particle size. Binding on the smallest particles of Au and Ni resulted in significant deformation from the initial truncated octahedron geometry.

THE UNIQUENESS OF SILVER

From the previous sections, it is apparent that Ag binds ethylene the weakest among the noble metals. Even the strongest binding sites for ethylene on Ag are still on the order of 0.2 eV lower than the next weakest metal, Au. Ag is unique for its weak chemisorption of ethylene.

This observation is consistent with analytical models of optimal binding energies for olefin separation membranes. The model of Pozun and Henkelman[13] predicts that the magnitude of selectivity increases with weaker chemisorption, as does the pressure at which the selectivity peak occurs. This model predicts

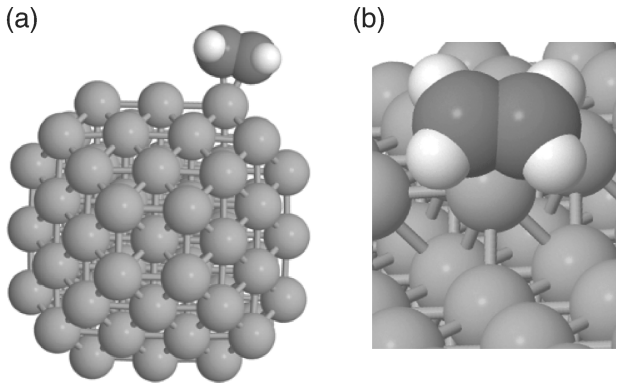

Figure 6. Ethylene binding (a) to a Ag_{79} corner and (b) to a kink site on Ag(111).

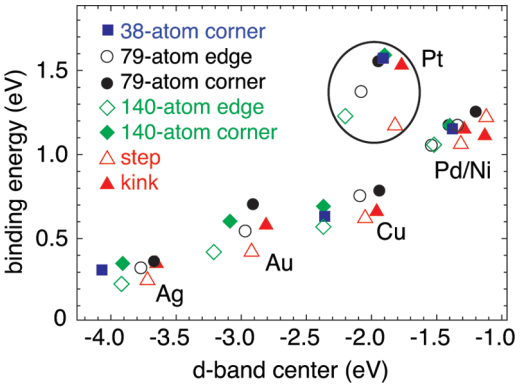

Figure 7. A correlation is found between the binding energy of ethylene at under-coordinated sites on non-Pt metals and their local *d*-band center.

Table 4. Corner and Kink Site Binding (eV)

	NP-38	NP-79	NP-140	slab-kink
Ni	*a*	1.26	1.34	1.12
Pd	1.15	1.18	1.17	1.16
Pt	1.57	1.56	1.59	1.54
Cu	0.63	0.79	0.69	0.67
Ag	0.31	0.37	0.35	0.36
Au	*a*	0.71	0.60	0.59

[a] Particle deformed.

that the maximum of selectivity occurs in a 50:50 ethylene/ethane gas mixture at a pressure given by

$$\frac{p}{p_0} = 2\exp\left(-\frac{\Delta E}{kT}\right) \quad (1)$$

where p_0 is the pressure at which half of the Langmuir adsorption sites are filled and ΔE is the ethylene binding energy. Optimal separation may be achieved more quickly if performed at higher pressures, so eq 1 predicts that the ideal binding should be low in order to maximize the pressure where peak selectivity occurs. This preference for weak chemisorption is consistent with our DFT calculations.

D-BAND MODEL FOR CHEMISORPTION

Several models of chemisorption explain binding trends as a function of the *d*-band of the metal. Newns and Anderson[43] describe the strength of chemisorption as a function of the adsorbent DOS, the discrete adsorbate binding state, and the coupling energy between the two. This model was expanded upon by Hammer and Nørskov in the tight-binding framework to establish a simple model for the *d*-band contribution to chemisorption.[44−46]

Using the notation of Hammer et al.,[45] the chemisorption strength between the *d*-band of the metal surface and the π and π^* orbitals of ethylene is given by

$$E_{chem} = -2\left[(1-f)\frac{V_\pi{}^2}{\varepsilon_d - \varepsilon_\pi} + fS_\pi V_\pi\right] - 2\left[f\frac{V_{\pi^*}{}^2}{\varepsilon_{\pi^*} - \varepsilon_d} + fS_{\pi^*}V_{\pi^*}\right] \quad (2)$$

In this expression, V is the coupling between the metal surface and the adsorbate state, ε_d is the *d*-band center, S is the overlap matrix element between the surface and ethylene states, and f is the *d*-band fractional filling. The *d*-bands of the noble metals, with the exception of Pt, are full,[47] so $f = 1$ for these metals.

This model predicts that, in the limit of small S, the energy difference between the unoccupied ethylene π^* orbital energy and the *d*-band center will be the controlling factor for chemisorption strength. As the *d*-band center approaches the Fermi level, $(\varepsilon_{\pi^*} - \varepsilon_d)$ becomes smaller, and the result is stronger chemisorption.

While DFT may be used to directly calculate binding energies, eq 2 provides a simplified estimate for the dominant factor in chemisorption strength. The binding energy of ethylene, as calculated using DFT, is plotted in Figure 7 against the local *d*-band center for corner and edge binding sites. The relevant nanoparticle binding positions are shown in Figure 1 with their bulk analogues shown in Figure 2. From Figure 7, there is a clear linear trend that, as the *d*-band center approaches the Fermi level, binding increases. All of the edge and corner sites all lie along the same linear scatter, with the exception of Pt.

In the case of Pt, the chemisorption strength is larger than that for the other metals at the same *d*-band center. The electronic structure of Pt is characterized by a wide, partially unfilled *d*-band with a filling factor, f, less than unity. For comparison, the *d*-bands of Pt and Pd are plotted in Figure 8. Due to the partial filling, the first term in eq 2 also contributes to the chemisorption and deviation from the linear relationship results.

As predicted by eq 2, an adsorbate interacting with a wide *d*-band that crosses the Fermi level results in strong binding by depopulating antibonding states and filling bonding states. The other metals—Cu, Ag, Au, Ni, and Pd—have *d*-bands of nearly the same width that lie entirely below the Fermi level. The common linear correlation of binding energy with *d*-band center among these metals is the result.

Bond Order and Normal Modes. Equation 2 predicts that charge is transferred both from the olefin π bond and into the π^* bond. Both of these interactions lower the C−C bond order and make the molecule closer to sp^3 hybridized than the gas phase sp^2 hybridization. The expectation for charge transfer and bond order weakening may be observed through the changes in the normal-mode frequencies of the chemisorbed ethylene.

As the C−C bond order decreases, each carbon center becomes increasingly sp^3-like rather than sp^2-like, and the ν(CC) stretch shifts proportionately with bond order. Correspondingly,

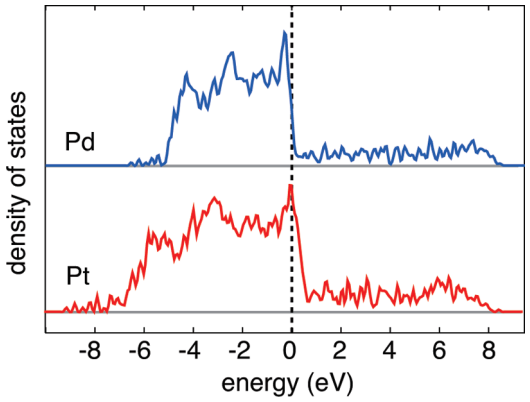

Figure 8. The total density of states for stepped slabs of Pt and Pd. The zero of energy is the Fermi level for each metal.

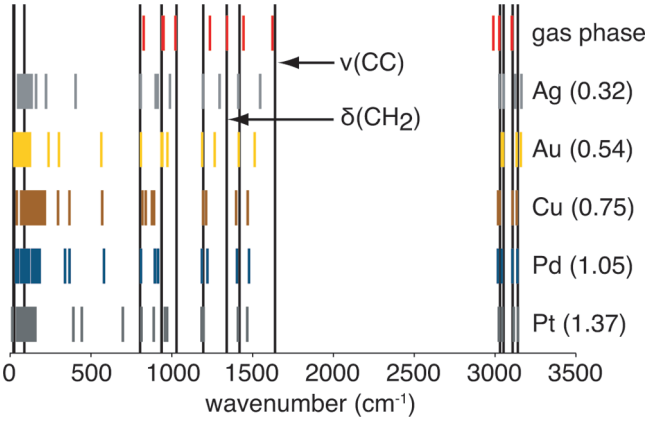

Figure 9. The normal modes of ethylene in the gas phase (long black lines) and chemisorbed on 79-atom corners (short colored lines) as calculated by DFT are compared to experimental gas phase data[49] (short red lines). In parentheses are the calculated binding energies in eV for the different metals.

the C−H bond angle becomes less than the 120° found in sp^2 carbon centers. This change in bond angle affects the Raman-active $\delta(CH_2)$ scissoring mode by shifting the frequency proportionately.

Due to the D_{2h} symmetry of ethylene, the ν(CC) and $\delta(CH_2)$ modes are infrared inactive; however, both modes are Raman active. Previous experimental Raman studies of ethylene bound on metal surfaces indicate that the chemisorbed species has a Raman shift in both of these modes corresponding to decreasing bond order.[48] A comparison of experimentally observed and calculated modes for pure ethylene is shown in the first row of Figure 9.

As predicted by DFT, experimental chemisorption of ethylene on noble metal electrodes indicates that Ag binds ethylene weaker than both Au and Cu.[50] The strength of ethylene chemisorption is observed experimentally with surface-enhanced Raman spectroscopy (SERS) to probe vibrational spectra. SERS indicates that the shift in the ν(CC) in chemisorbed ethylene similarly indicates that silver binds ethylene weaker than both gold and copper.[48]

OPTIMIZING OLEFIN/PARAFFIN SEPARATION MEMBRANES

With respect to the design of olefin/paraffin separation membranes, analytical models[13] indicate that an increased active surface area and weak chemisorption are desirable. Small particles have a favorable surface/volume ratio, and Tables 3 and 4 indicate that the binding energy on Ag does not change significantly with particle size. Table 1, however, indicates that there is no chemisorption on the Ag(111) face at any size. This result indicates that all of the selectivity that occurs from Ag nanocomposite membranes is due to under-coordinated sites or defects. One criterion for improving upon Ag in nanocomposite membranes is a (111) face that weakly chemisorbs ethylene.

The other late transition metals follow the trends identified in Figure 7 where the *d*-band is the controlling factor. Importantly, there is no crossover point—with the exception of Ni and Pd, which have similar *d*-band centers—where one metal becomes more reactive than another. This result simply indicates that, while size may be tuned toward smaller particles, small particles of Cu group metals do not become more reactive than the bulk values of the Ni group. Size effects alone are not pronounced enough to drastically shift the binding energies toward weak binding.

Bimetallic systems are of particular interest due to the tunable nature of the properties. For example, Khan et al. have shown experimentally that a Ni monolayer on Pt(111) or a Pt monolayer on Ni(111) is more catalytically active for cyclohexene hydrogenation than either Pt(111) or Ni(111).[51] Differences in lattice constants and *d*-band structures alter the surface electronic properties, and this interaction may be tuned to optimize a given interaction. Tuning the nanoparticle−olefin interaction with bimetallic systems offers promise of enhanced olefin−paraffin separation membranes.

CORE−SHELL NANOPARTICLES

Core−shell nanoparticles offer tunable control over electronic and structural properties. Binding energies on a core−shell system are adjusted from the behavior of the pure metal systems through both electronic and geometric effects. Lattice constant mismatch introduces strain into the shell overlayer.

Bulk lattice constants follow the trend Pd < Pt < Ag < Au. The choice of core metal introduces compression or strain into the shell. The ratio of shell to core lattice constants, which are taken from Wang et al.,[27] is used to determine compression or expansion. When the ratio is less than 1, the shell is streched due to a larger lattice constant in the core.

As described by Mavrikakis et al., when the surface is compressed, the local *d*-band width increases and the center of the band moves down in energy in order to keep the same overall filling.[52,53] This trend in *d*-band center due to lattice mismatch in core−shell nanoparticles is shown in Figure 10.

When Au or Ag is used as a core for Pd or Pt, the shell *d*-band center becomes closer to the Fermi level. Both Ag@Pt and Au@Pt have *d*-band centers that are on the order of 0.2 eV—a 10% shift—closer to the Fermi level than the case of Pd@Pt. Similarly, a smaller core, the cases of Pt@Ag and Pt@Au, results in the surface *d*-band center shifting downward but to a lesser extent.

Edges and Corners. The effect on edge and corner site chemisorption that results from changing the identity of nanoparticle cores is shown in Tables 5 and 6. The trends in binding energy, however, do not follow the predictions of the Hammer−Nørskov model given the surface *d*-band shifts that appear in Figure 10.

The trends in the binding energies indicate that the surface *d*-band center alone does not have predictive power for the ethylene

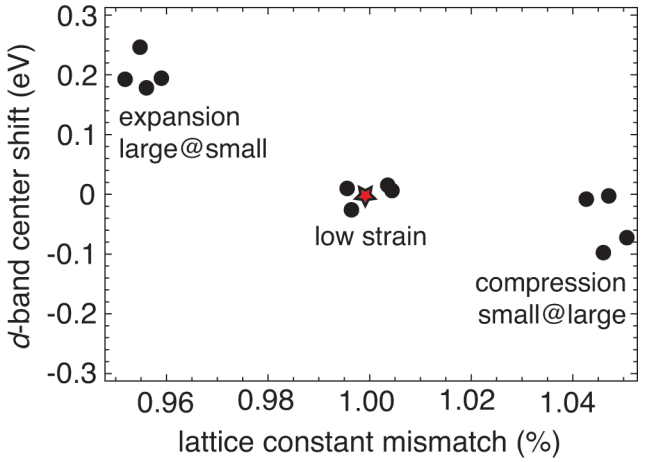

Figure 10. The *d*-band shifts from pure metal nanoparticles are shown as a function of the ratio of shell to core metal lattice constants. The red star denotes the unshifted pure metal cases.

Table 5. Ethylene Binding on 79-Atom Core−Shell Nanoparticle Edge Sites (eV)

	core metal			
shell metal	Pd	Pt	Ag	Au
Pd, π	1.21	1.22	1.01	1.14
Pd, di-σ	1.40	1.35	1.34	1.47
Pt, π	1.23	1.36	1.03	1.37
Pt, di-σ	1.77	1.72	1.71	1.92
Ag, π	0.31	0.39	0.32	0.40
Ag, di-σ	0.23	0.28	*a*	0.32
Au, π	0.53	0.58	0.39	0.54
Au, di-σ	0.28	0.44	0.27	0.56

[a] No stable binding site.

Table 6. Ethylene Binding on 79-Atom Core−Shell Nanoparticle Corner Site (eV)

	core metal			
shell metal	Pd	Pt	Ag	Au
Pd	1.16	1.25	1.16	1.25
Pt	1.58	1.54	1.42	1.64
Ag	0.41	0.45	0.37	0.49
Au	0.61	0.64	0.49	0.70

binding energy. For instance, the binding energies of Ag-cored particles are always the lowest for a given shell metal. This result is the opposite of the predictions of the Hammer−Nørskov *d*-band model and of eq 2.

Ag has a larger lattice constant than Pd and Pt, so the Hammer−Nørskov model predicts that the binding energy should increase due to the *d*-band shift, yet the opposite is observed. In addition, Au has a larger lattice constant than Ag, but the Au cored particles do not follow the same trends as Ag cores. Although lattice constant mismatch can predict the shell *d*-band shift, it does not predict corresponding shifts in the binding energy.

In terms of other factors impacting local reactivity, nearest neighbors in metal layers have been identified with a strong influence on reactivity. In the case of Pd on Au, Roudgar and Gross have identified two Pd overlayers on bulk Au as the maximum of surface reactivity for reactions limited by CO or H binding.[54] With a single overlayer, the surface *d*-band is shifted toward the Fermi level, but the relatively inert Au bulk overlaps poorly with the Pd overlayer and does not contribute or accept much charge during chemisorption.

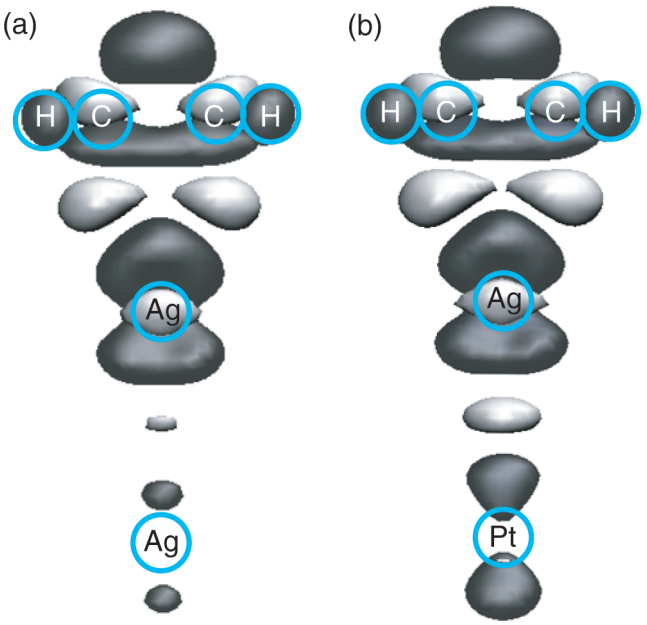

Figure 11. The ethylene binding-induced charge redistribution on (a) a pure Ag_{79} nanoparticle and (b) a Pt@Ag nanoparticle. The dark charge-difference isosurfaces are regions of depleted charge, and the light isosurfaces have added charge. The symmetry of the charge-difference isosurfaces shows that charge is transferred from the π orbital to the π^* orbital on ethylene.

Tables 5 and 6 demonstrate that substituting Ag as a core will lower the binding energy, despite its large lattice constant that expands the shell and raises the surface *d*-band. The importance of sublayer nearest-neighbors is demonstrated in Figure 11 where ethylene binds stronger on Pt@Ag than on pure Ag as a result of the Pt core. The Pt core, as shown in Figure 11, more readily facilitates charge transfer. During this charge redistribution upon binding, the subsurface nearest neighbors play a large role in donating or accepting charge, and this interaction directly affects the strength of chemisorption at the surface.

The implication for tuning Ag nanoparticles for olefin/paraffin separation membranes is that the binding energy may be tuned upward by introducing a different metal into the core. The binding energy, however, may not be tuned lower, because Ag is the most inert metal in terms of olefin binding. Nanoparticles of Ag@Au, however, have lower binding energies than pure Au and bind ethylene in the same regime as pure Ag.

Facets of Core−Shell Nanoparticles. In addition to tuning binding downward on reactive nanoparticles, a reasonable goal to improve olefin/paraffin separation membranes is to activate the (111) faces of Ag-shelled nanoparticles. As shown in Table 7, however, no Ag-shelled particles bind ethylene.

Similar to the effects on edges and corners, Table 7 demonstrates that, as a core, Ag may be used to tune the binding energy downward. For the π binding geometry, the binding energy on Ag@Pd and Ag@Pt is weaker than that on pure Pd and Pt,

Table 7. Ethylene Binding on 79-Atom Core−Shell Nanoparticle (111) Faces

	core metal			
shell metal	Pd	Pt	Ag	Au
Pd, π	0.87	0.89	0.77	0.99
Pd, di-σ	1.10	1.11	1.15	1.30
Pt, π	1.02	1.37	0.92	1.11
Pt, di-σ	1.43	1.73	1.37	1.70
Ag	*a*	*a*	*a*	*a*
Au	0.12	0.12	0.22	0.25

[a] No chemisorption >0.05 eV.

Table 8. Ethylene Binding on 25%-75% Au−Ag Random Alloys (eV)

	edge		corner		(111)	
size	Au	Ag	Au	Ag	Au	Ag
NP-79	0.28	0.33	0.33	0.41	*a*	0.15
NP-140	0.21	0.28	0.30	0.37	*a*	0.11
slab	0.23	0.30	0.37	0.40	*a*	0.10

[a] No chemisorption >0.05 eV.

respectively. Although binding is slightly weaker for Ag@Au than it is for pure Au, the (111) face remains active. Given that the edge and corner sites for this particle are tuned downward into the regime of pure Ag binding energies, this result suggests that Ag@Au nanoparticles have the promise of a weak interaction with ethylene on under-coordinated atoms without the drawback of inactive (111) faces.

CHEMISORPTION ON AG(111) ALLOYS

Au and Ag have been demonstrated to form stable random alloyed nanoparticles at various mole fractions of each component without lattice strain.[19,55,56] In contrast to particles with independent Ag and Au phases that display two plasmon resonances, random alloys of Au−Ag display a single plasmon peak whose position varies linearly with mole fraction.[57] Nanoparticles of these alloys offer an additional parameter—the mole fraction of each component—to tune.

Random structures for 25%−75% Au−Ag alloys were generated for each binding site, with at least six random structures where ethylene would bind on a Ag atom and at least six structures with binding on a Au atom. The average binding energy was taken for binding on each atom type. Random alloys of $Au_{10}Ag_{28}$, similar to the behavior of Au_{38} in Table 4, tended to deform upon binding and were excluded.

The trends in Table 8 for chemisorption on the Au−Ag random alloys are different from the trends in the Ag@Au core−shell nanoparticle. In particular, binding on Au atoms is lowered from the pure Au case and, surprisingly, the Ag@Au case. The binding energies on these sites are on the order of the binding energy on a similar Ag atom. The net effect is that the edges of these alloy particles will bind ethylene with approximately the same binding energy as a pure Ag particle.

Unlike pure Ag particles, which do not chemisorb ethylene on (111) faces at any particle size, the Au−Ag alloyed particles in Table 8 have active (111) faces that bind ethylene at all sizes. The reactivity of the Ag atoms on the (111) face is enough to activate the full surface regardless of nanoparticle size. One of the primary goals in replacing pure Ag nanoparticles in olefin/paraffin membranes is to increase the amount of active surface area on each particle that will chemisorb ethylene. The Au−Ag 25%−75% random alloy nanoparticles maintain an effective binding energy on under-coordinated sites while activating the previously inactive (111) faces.

CONCLUSIONS

Silver, the metal most commonly used in nanocomposite membranes for olefin−paraffin separations, has been demonstrated to have the weakest binding energy for ethylene among all of the late transition metals. Analytical modeling has demonstrated that, in general, weak chemisorption of ethylene is preferable in membranes and that the amount of active metal surface area in a membrane is a crucial factor. Thus, we have sought to identify the tunable parameters that may be used to activate the (111) faces of silver nanoparticles without significantly strengthening the binding energy on edges and corners.

We identify the *d*-band as the controlling factor in chemisorption on pure metals. The *d*-band center does not shift far enough as a function of nanoparticle size to significantly affect chemisorption. The binding interaction during chemisorption depletes charge from the C−C π bond and lowers the bond order. We demonstrate that the ν(CC) and $\delta(CH_2)$ modes of ethylene shift proportionately with binding energy. These modes are Raman-active and Cu, Au, Ag, and bimetallics of these metals are all active SERS substrates.

We have demonstrated that tuning for nanoparticle size alone is not enough to activate the (111) faces on small Ag particles. Small particles of Au have active (111) faces; however, these small particles have unfavorably strong binding on edges and corners. Larger particles of Cu, despite having an unfavorable surface−volume ratio, display trends in binding energy that also indicate potential for use in nanocomposite membranes.

In bimetallic systems, structure is a tunable parameter in which unordered random alloys and ordered core−shell nanoparticles may both be generated experimentally. We have identified subsurface atoms as playing a large role in binding energies for ethylene. Although the *d*-band shift in the surface due to core−shell lattice mismatch plays a role in chemisorption, the ability of the subsurface layers to donate or accept charge has a significant impact on binding energies. Substituting reactive metals into a Ag shell has been demonstrated to not activate the Ag(111) faces. Ag cores, however, lower the binding energies on reactive particles, and we identify Ag@Au as a strong candidate for use in olefin/paraffin separation membranes.

We find that random alloys of Ag and Au display the most promise for use in nanocomposite membranes. Alloys of 75% Ag with 25% Au display binding energies that are comparable to the pure Ag binding energies on edges and corners. The (111) faces of these alloys display increased reactivity over the reactivities of both pure Au and Ag for all particle sizes and in the bulk. We expect that nanoparticles of this random alloy will be stable over time under industrial operating conditions and chemisorb ethylene on (111) faces as well as under-coordinated sites. Particles of this composition will bind ethylene in the same way that pure Ag does but without the drawback of inactive surface area.

AUTHOR INFORMATION

Corresponding Author
*E-mail: henkelman@mail.utexas.edu.

ACKNOWLEDGMENT

This work was supported by the National Science Foundation NIRT Award No. 0708779. Computing resources were provided through the Texas Advanced Computing Center and through the Freshman Research Initiative (FRI) at the University of Texas at Austin. A.S. was supported by a FRI summer research fellowship. R.H.S. was supported through the Welch Summer Scholars Program at the University of Texas at Austin.

REFERENCES

(1) Wang, H. T.; Lin, D. M.; Zhou, X. P. *Appl. Catal., A* **2009**, *364*, 130–136.
(2) Ren, T.; Patel, M.; Blok, K. *Energy* **2006**, *31*, 425–451.
(3) Ren, T.; Patel, M. K.; Blok, K. *Energy* **2008**, *33*, 817–833.
(4) Eldridge, R. B. *Ind. Eng. Chem. Res.* **1993**, *32*, 2208–2212.
(5) Kang, Y. S.; Kim, J. H.; Won, J.; Kim, H. S. In *Materials Science of Membranes for Gas and Vapor Separation*; Yampolskii, Y., Pinnau, I., Freeman, B., Eds.; John Wiley & Sons Ltd.: West Sussex, UK, 2006; Chapter 16, pp 391−410.
(6) Ho, W. S.; Dalrymple, D. C. *J. Membr. Sci.* **1994**, *91*, 13–25.
(7) Morisato, A.; He, Z.; Pinnau, I.; Merkel, T. C. *Desalination* **2002**, *145*, 347–351.
(8) Pinnau, I.; Toy, L. G. *J. Membr. Sci.* **2001**, *184*, 39–48.
(9) Kim, H. S.; Ryu, J. H.; Kim, H.; Ahn, B. S.; Kang, Y. S. *Chem. Commun.* **2000**, *14*, 1261–1262.
(10) Kang, S. W.; Char, K.; Kang, Y. S. *Chem. Mater.* **2008**, *20*, 1308–1311.
(11) Kang, S. W.; Lee, D. H.; Park, J. H.; Char, K.; Kim, J. H.; Won, J.; Kang, Y. S. *J. Membr. Sci.* **2008**, *322*, 281–285.
(12) Kang, S. W.; Hong, J.; Park, J. H.; Mun, S. H.; Kim, J. H.; Cho, J.; Char, K.; Kang, Y. S. *J. Membr. Sci.* **2008**, *321*, 90–93.
(13) Pozun, Z. D.; Henkelman, G. *J. Membr. Sci.* **2010**, *364*, 9–16.
(14) Froemming, N. S.; Henkelman, G. *J. Chem. Phys.* **2009**, *131*, 234103.
(15) Valden, M.; Lai, X.; Goodman, D. W. *Science* **1998**, *281*, 1647–1650.
(16) Besenbacher, F.; Chorkendorff, I.; Clausen, B. S.; Hammer, B.; Molenbroek, A. M.; Nørskov, J. K.; Stensgaard, I. *Science* **1998**, *279*, 1913–1915.
(17) Greeley, J.; Mavrikakis, M. *Nat. Mater.* **2004**, *3*, 810–815.
(18) Scott, R. W. J.; Wilson, O. M.; Oh, S.-K.; Kenik, E. A.; Crooks, R. M. *J. Am. Chem. Soc.* **2004**, *126*, 15583–15591.
(19) Wilson, O. M.; Scott, R.W. J.; Garcia-Martinez, J. C.; Crooks, R. M. *J. Am. Chem. Soc.* **2005**, *127*, 1015–1024.
(20) Kresse, G.; Hafner, J. *Phys. Rev. B* **1993**, *47*, 558–561.
(21) Hohenberg, P.; Kohn, W. *Phys. Rev.* **1964**, *136*, 864–871.
(22) Kohn, W.; Sham, L. J. *Phys. Rev.* **1965**, *140*, 1133–1138.
(23) Blöchl, P. E. *Phys. Rev. B* **1994**, *50*, 17953–17979.
(24) Kresse, G.; Joubert, D. *Phys. Rev. B* **1999**, *59*, 1758–1775.
(25) Perdew, J. P.; Wang, Y. *Phys. Rev. B* **1992**, *45*, 13244–13249.
(26) Holender, J. M.; Gillan, M. J.; Payne, M. C.; Simpson, A. D. *Phys. Rev. B* **1995**, *52*, 967–975.
(27) Wang, Y.; Curtarolo, S.; Jiang, C.; Arroyave, R.; Wang, T.; Ceder, G.; Chen, L.-Q.; Liu, Z.-K. *CALPHAD: Comput. Coupling Phase Diagrams Thermochem.* **2004**, *28*, 79–90.
(28) Monkhorst, H. J.; Pack, J. D. *Phys. Rev. B* **1976**, *13*, 5188–5192.
(29) Methfessel, M.; Paxton, A. T. *Phys. Rev. B* **1989**, *40*, 3616–3621.
(30) Bader, R. *Atoms in Molecules: A Quantum Theory*; Oxford University Press: Oxford, UK, 1990.
(31) Tang, W.; Sanville, E.; Henkelman, G. *J. Phys.: Condens. Matter* **2009**, *21*, 084204.
(32) Mills, G.; Gordon, M. S.; Metiu, H. *J. Chem. Phys.* **2003**, *118*, 4198–4205.
(33) Skibbe, O.; Vogel, D.; Binder, M.; Pucci, A.; Kravchuk, T.; Vattuone, L.; Venugopal, V.; Kokalj, A.; Rocca, M. *J. Chem. Phys.* **2009**, *131*, 024701.
(34) Kokalj, A.; Corso, A. D.; de Gironcoli, S.; Baroni, S. *Surf. Sci.* **2002**, *62*−*68*, 507–510.
(35) Bocquet, M.-L.; Rappe, A. M.; Dai, H.-L. *Mol. Phys.* **2005**, *103*, 883–890.
(36) Windham, R. G.; Bartram, M. E.; Koel, B. E. *J. Phys. Chem.* **1988**, *92*, 2862–2870.
(37) Ge, Q.; King, D. A. *J. Chem. Phys.* **1999**, *110*, 4699–4702.
(38) Mittendorfer, F.; Thomazeau, C.; Raybaud, P.; Toulhoat, H. *J. Phys. Chem. B* **2003**, *107*, 12287–12295.
(39) Pallassana, V.; Neurock, M.; Lusvardi, V. S.; Lerou, J. J.; Kgraten, D. D.; van Santen, R. A. *J. Phys. Chem. B* **2002**, *106*, 1656–1669.
(40) Pichierri, F.; Iitaka, T.; Ebisuzaki, T.; Kawai, M.; Bird, D. M. *J. Phys. Chem. B* **2001**, *105*, 8149–8154.
(41) Bernardo, C. G. P. M.; Gomes, J. A. N. *J. Mol. Struct. (THEOCHEM)*, *542*, 263−271.
(42) Kokalj, A.; Corso, A. D.; de Gironcoli, S.; Baroni, S. *J. Phys. Chem. B* **2002**, *106*, 9839–9846.
(43) Newns, D. M. *Phys. Rev.* **1969**, *178*, 1123–1135.
(44) Hammer, B.; Nørskov, J. K. *Nature* **1995**, *376*, 238–240.
(45) Hammer, B.; Morikawa, Y.; Nørskov, J. K. *Phys. Rev. Lett.* **1996**, *76*, 2141–2144.
(46) Hammer, B. *Top. Catal.* **2006**, *37*, 3–16.
(47) Fuster, G.; Tyler, J. M.; Brener, N. E.; Callaway, J. *Phys. Rev. B* **1990**, *42*, 7322–7329.
(48) Akemann, W.; Otto, A. *Langmuir* **1995**, *11*, 1196–1200.
(49) Shimanouchi, T. In *NIST Chemistry WebBook, NIST Standard Reference Database Number 69*; Linstrom, P. J., Mallard, W. G., Eds.; National Institute of Standards and Technology: Gaithersburg, MD; http://webbook.nist.gov (retrieved Aug 16, 2010).
(50) Mrozek, M. F.; Weaver, M. J. *J. Phys. Chem. B* **2001**, *105*, 8931–8937.
(51) Khan, N. A.; Zellner, M. B.; Murillo, L. E.; Chen, J. G. *Catal. Lett.* **2004**, *95*, 1–6.
(52) Mavrikakis, M.; Hammer, B.; Nørskov, J. K. *Phys. Rev. Lett.* **1998**, *81*, 2819–2822.
(53) Ruban, A.; Hammer, B.; Stoltze, P.; Skriver, H.; Nørskov, J. K. *J. Mol. Catal. Chem.* **1997**, *115*, 421–429.
(54) Roudgar, A.; Gross, A. *Phys. Rev. B* **2003**, *67*, 033409.
(55) Link, S.; Wang, Z. L.; El-Sayed, M. A. *J. Phys. Chem. B* **1999**, *103*, 3529–3533.
(56) Shibata, T.; Bunker, B. A.; Zhang, Z.; Meisel, D.; Vardeman, C. F., II; Gezelter, J. D. *J. Am. Chem. Soc.* **2002**, *124*, 11989–11996.
(57) Raveendran, P.; Fu, J.; Wallen, S. L. *Green Chem.* **2006**, *8*, 34–38.